Chapter 6

Polymer-NASICON composites as electrolyte for ASSCs

In chapters 3-5, we have discussed Li^+ and Na^+ ion conducting polymer-NASICON composites in which conductivity could be enhanced to ~ 10^{-4} $\Omega^{-1}cm^{-1}$ particularly in a 'solid state'. Looking at the appreciable rise in Na^+ ion based composites, more attention is given to them in this chapter for supercapacitor applications. Further, no work, to our knowledge, has been done on Na^+ ion supercapacitors particularly using solid polymer electrolytes. Thus, the chapter presents applications of developed Na^+ ion based hybrid polymer-NASICONs as the electrolyte in all-solid-state supercapacitor (ASSC). Since it is the first study of its kind, it also examines suitable current collector (copper versus graphite) for the Na^+ ion ASSCs. Preliminary investigations on all-solid-state pseudocapacitors are also presented. Chapter also attempts to comprehend the tentative mechanism for charge storage.

Results Published in M. D. Singh, G. Kaur, S. Sharma and A. Dalvi, "*All-solid-state flexible Na^+ ion supercapacitors using NASICON-polymer hybrids electrolyte*" Journal of energy storage 41 (2021) 102984.

6.1 Electrical double layer capacitor (EDLC)

Using optimized compositions in 10NaI-90[PEO1-xNZSPx] with high ionic conductivity, EDLCs were fabricated in a 2032 coin cell assembly in the following configuration where AC refers to activated carbon.

(i) AC|0 NZSP|AC, where 0 NZSP refers to x = 0

(ii) AC|40 NZSP|AC, where 0 NZSP refers to x = 0.4

(iii) AC|70 NZSP|AC, where 0 NZSP refers to x = 0.7

The performance of the resultant 2032 cells was further investigated.

6.1.1 Activated carbon (AC)electrode:

Before the EDLC fabrication, the surface area, pore diameter, and distribution of the AC were studied using the BET diagram. Fig. 6.1a shows N_2 adsorption-desorption isotherm curve of type I for the activated carbon [1][2].

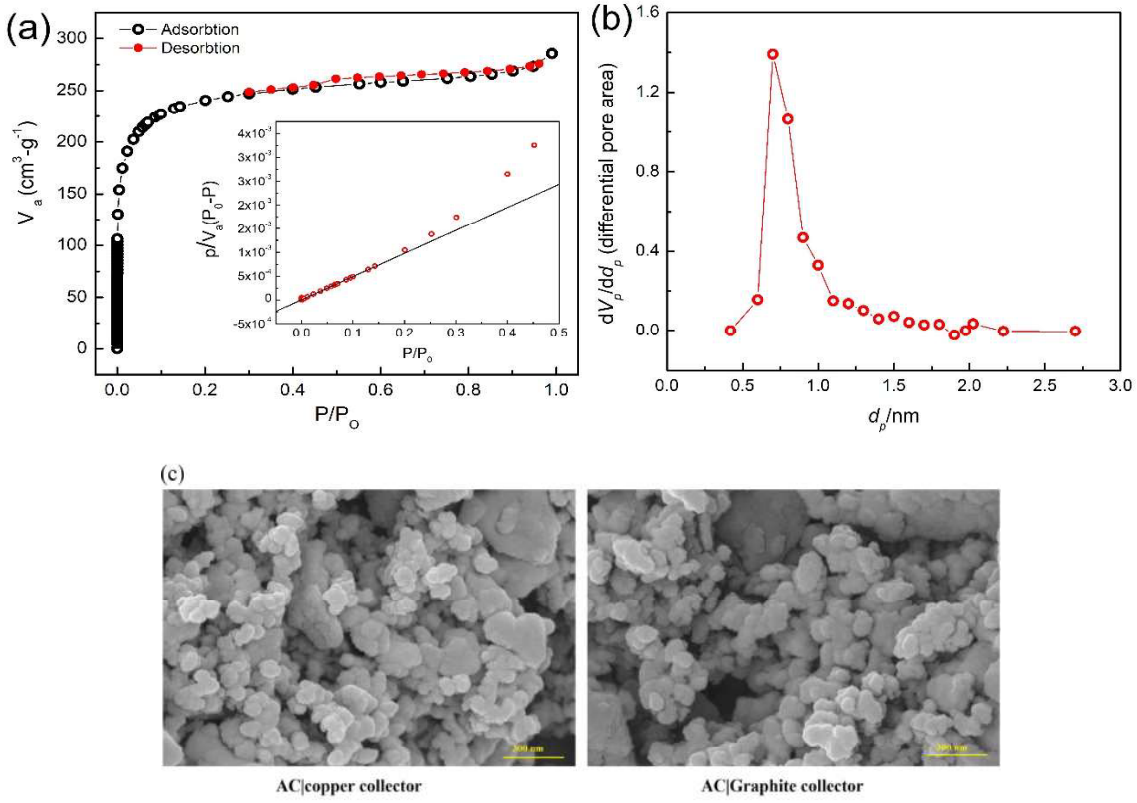

Fig. 6.1 *(a) Nitrogen adsorption-desorption isotherm curve of the activated carbon (inset: linear fitting with BET equation), (b) Micropore distribution plot of the activated carbon and, (c) FESEM images for the deposited AC electrode on copper and graphite current collectors.*

As observed in Fig. 6.1a, at the lower relative pressure ($P/P_0 \leq 0.0005$), the adsorption isotherm curve rises steeply, followed by a gradual rise tending to saturation at a higher relative pressure ($0.2 \leq P/P_0 \leq 0.9$). The step rise ($P/P_0 \leq 0.0005$) suggests the presence of a significant amount of micropores (< 2 nm). In addition, the presence of mesopores is also evident as the isotherm gradually reaches above $P/P_0 \geq 0.01$. Fig. 6.1b shows micropores (MP) distribution plot for activated carbon. Pore size distribution was calculated using BJH method [3]. The total pore volume (V_p) and average pore diameter (V_d), for the samples under study, is found to be 0.39 cm^3g^{-1} and 1.58 nm, respectively. Moreover, the specific surface area calculated from the linear form of the BET equation (inset of Fig. 6.1a) is found to be ~ 877 m^2-g^{-1}. As also evident, the particle and pores size of deposited carbon is homogeneously distributed (Fig. 6.1c). This further suggests the suitability of as-prepared activated carbon for electrode applications.

6.1.2 Cell performance:

Since the NZSP-polymer hybrid solid electrolyte films were used for the first time for the EDLC application, two different current collectors were used to examine their compatibility with the thin film electrolytes. The electrochemical performance of the cell with two different current collectors (copper and graphite) was studied at a temperature just before melting of the polymer (at ~ 40°C).

The optimal voltage for the cell operation was obtained from cyclic voltammetry scans. Fig. 6.2 a and b, show CV scans for cell with configuration: AC|10NaI_90[$PEO_{1-x}NZSP_x$]|AC, where x = 0, 0.4 and 0.7 (term as cell 1, cell 2 and cell 3 for x = 0, 0.4 and 0.7, respectively), recorded at 10 mV-s^{-1} scan rate. As evident in Fig. 6.2, the optimal voltage for cell with x = 0, 0.4 and 0.7 is found to be ~ 2V. The absence of any prominent reduction and oxidation peak readily suggests the formation of EDLC. Further, Nyquist plots (0.1 mHz - 2 MHz) of the cell (inset of Fig. 6.2a and b) exhibit only a lower frequency spike that again suggests a predominant capacitive nature of the cells. Interestingly, unlike 0 NZSP compositions, the CV cycle for cell 2 (with 40NZSP solid electrolyte) shows a relatively larger area under the characteristics I-V curve and exhibits a box-like (though quasi rectangular) nature. The area under the curve corresponds to the total charge stored in the cell. Evidently, the NASICON content in the polymer plays a role here. The cell with 70 NZSP electrolyte though exhibits lesser area under the CV curves, despite the highest ionic conductivity of this composition. In

EDLC configuration, the charge transport mechanism is most likely due to adsorption or electric double layer formation at the electrode-electrolyte interface. Thus, the surface morphology of the electrolyte would play a significant role in charge storage or transport mechanism.

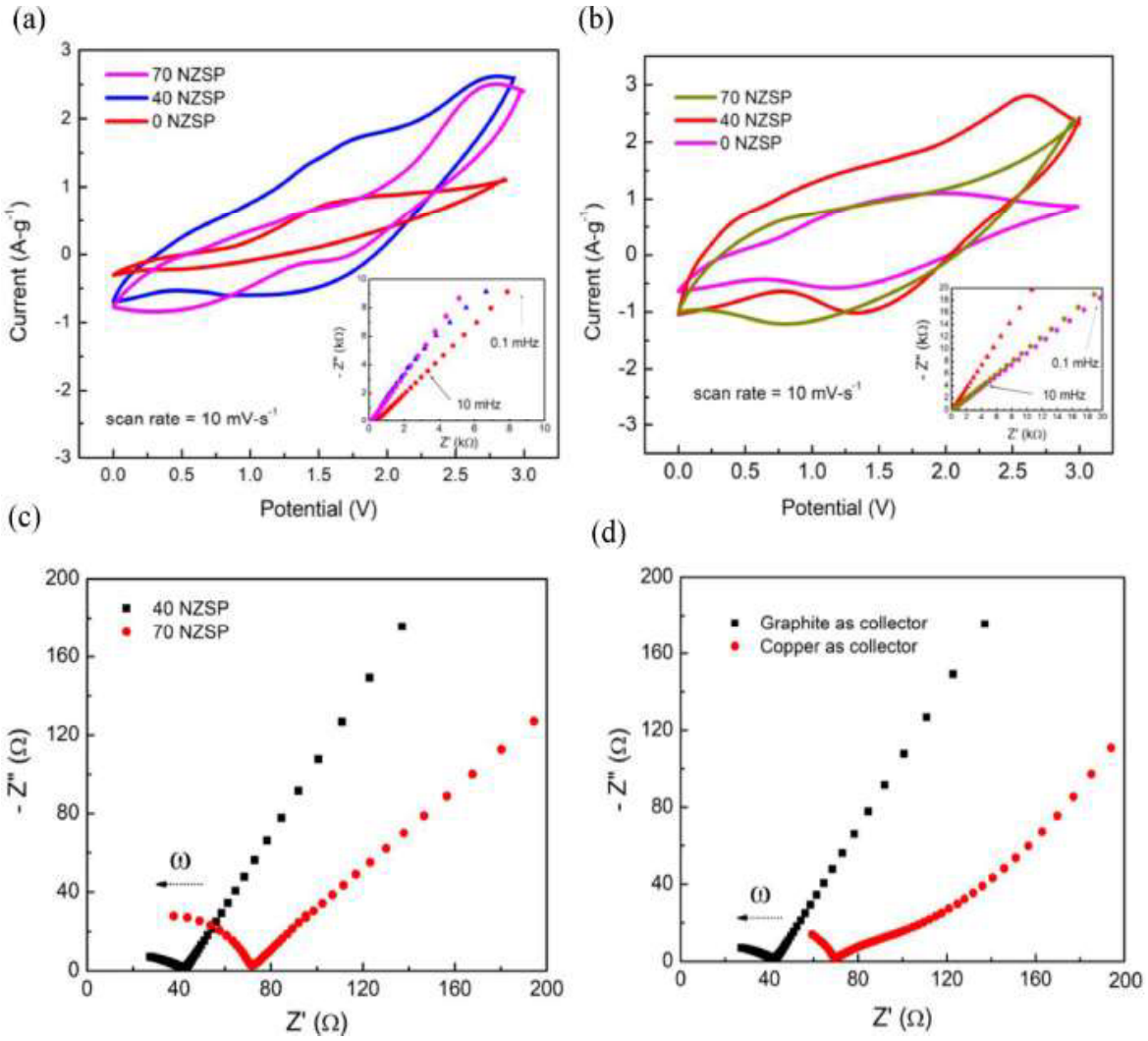

Fig. 6.2 *CV of EDLC cells (10mV-s^{-1}) with configuration of AC\|10NaI-[PEO$_{1-x}$NZSP$_x$]\|AC where x = 0, 0.4 and 0.7 using (a) copper and (b) graphite as current collectors. Inset: corresponding Nyquist plots. (c) Nyquist plot for the device with 40 and 70 NZSP with Graphite as a current collector. (d) Nyquist plot for the device with 40 NZSP electrolyte for graphite and copper collector*

As evident in the SEM image (Chapter 4, Fig. 4.11b), the composite with 70 NZSP shows a relatively rough and inhomogeneous surface as compared to 40 NZSP. More ceramic crystallites on the surface possibly establish poor contact with activated carbon thus adsorption of electrolyte ions is prevented. The SEM image (Chapter 4, Fig. 4.11b) does suggest NASICON crystallites occupying the surface.

Further, it is also expected that poor interfacial contact would enhance interfacial impedance. The same has been observed in the Nyquist plot (shown in an extended scale) where 70 NZSP shows higher resistance as compared to 40 NZSP in device configuration (Fig. 6.2c). Nevertheless, the 70 NZSP solid electrolyte is highly conducting ($\sigma \sim 10^{-4}\ \Omega^{-1}cm^{-1}$ at 30°C) and more efforts are required to improve the contact area.

As again evident in Fig. 6.2a and b, ASSC cells with copper and graphite as a collector exhibit similar CV characteristics. If compared, the cell with graphite collector exhibits relatively better current capacity ($A\text{-}g^{-1}$), possibly due to better contact of the activated carbon with the graphite sheet. Contact resistance is directly related to the nature of the current collector as reported earlier [4]. As also revealed previously [5], poor adhesion of carbon material to copper surface leads to the formation of a resistive intrinsic oxide layer. Fig. 6.2d shows a typical Nyquist plot, on an extended scale for EDLCs with graphite and copper current collectors for 40NZSP as electrolytes. As evident, the cell with graphite collector exhibits lower contact resistance.

The cells with 40 NZSP as electrolyte were further studied to examine the possible mechanism of EDLC formation. CV scans and gravimetric charging-discharging cycles (at 40°C) at different currents are shown in Fig. 6.3. The CV at different scan rates with copper and graphite collector is shown in Fig. 6.3a and b, respectively. The current density (Fig. 6.3a) increases with higher scan rates. The CV scans also show box-like behavior at least up to ~ 2V, typical characteristic behavior of EDLCs [1,6,7].

It is interesting to analyze the mechanism of energy storage in these EDLCs. No prominent redox peak is evident in the cyclic voltammogram upto 2V. Nyquist plots (inset of Fig. 6.2b where steep vertically rising impedance behavior at low frequencies) suggest that the charge transport mechanism is well governed by the formation of electric double layer at the electrode-electrolyte interface (inset, Fig. 6.2a and b). The absence of redox peaks in the CV scans also

suggests that the charge carriers in the electrolyte physically adsorbed at the electrode (activated Carbon) and responsible for charge storage.

It is likely that the Na^+ as well as I^- ion takes part in EDLC formation, as a charge storage ion. The activity of mobile ions at the interface should be directly related to the transport number of mobile ions in the electrolyte. Normally, in a typical polymer-based electrolyte anion transport number is prominent [8][9][10]. Thus, in response to the external electric field, anions in the electrolyte should also contribute to electric double layer formation at the interface.

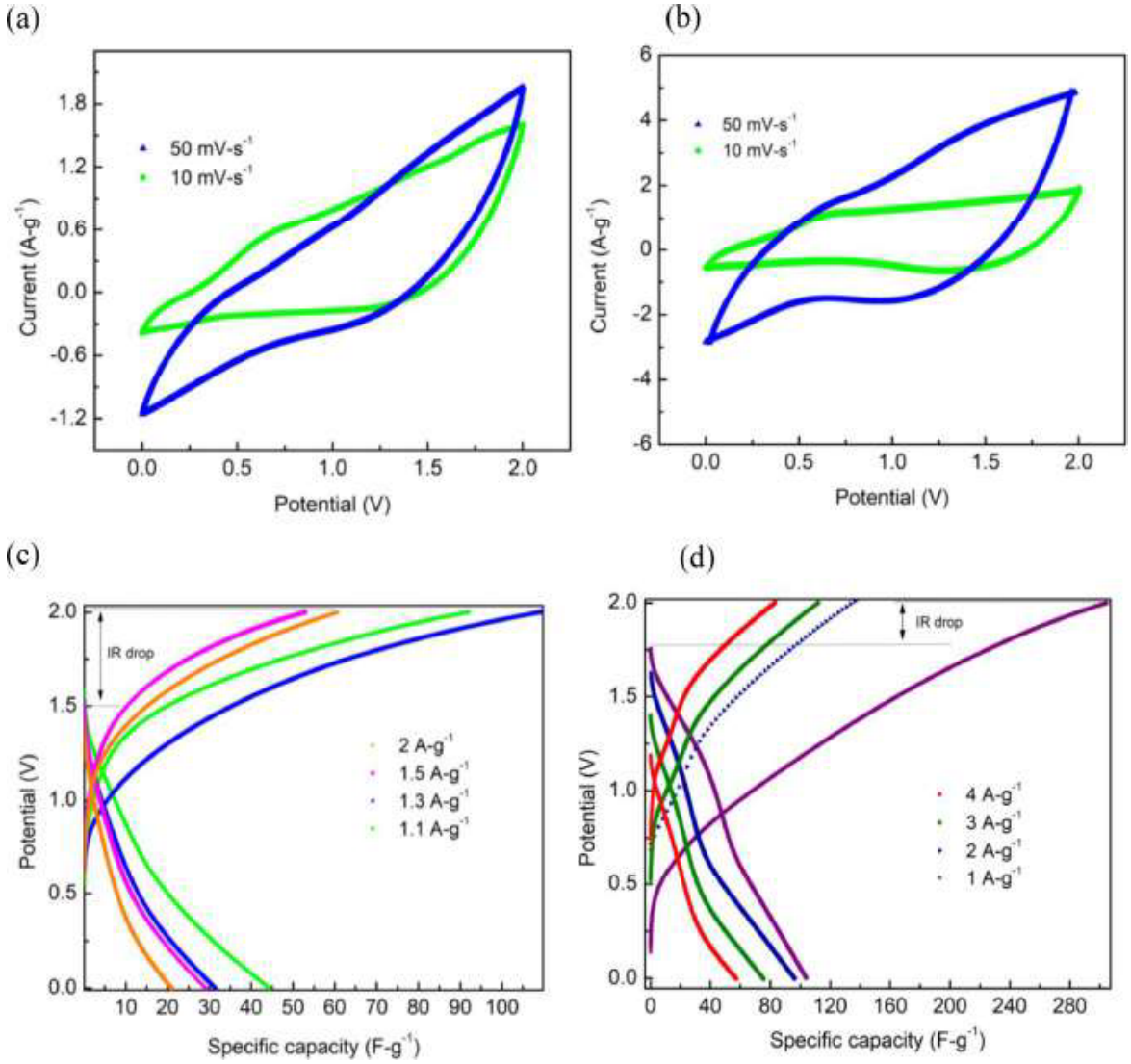

Figure 6.3 *CV scans at 10 and 50 mV-s^{-1} for EDLCs with 40 NZSP composite as electrolyte with (a) copper and (b) graphite current collectors; specific charge-discharge capacitance at different current densities for EDLCs with (c) copper and (d) graphite current collectors.*

As discuss in chapter 4, NASICON content in the matrix significantly influence the cation transport number in these composites [8][9][10]. Such results suggested that with the increase of NASICON content, cation transport number exhibits a substantial rise. Thus with NASICON addition in the matrix, I^- ion contribution as a storage ion may reduce. Particularly for a large content of NASICON in the matrix, cations play important role in charge storage.

For the EDLCs with 40 NZSP as electrolyte, possibly Na^+ as well as I^- ions contribute to double layer formation. Nevertheless, the role of Na^+ ion in the EDLC formation should be prominent. The Na^+ ion is known to have a higher diffusion coefficient and mobility than any of its counter anion [11]. Therefore, it can quickly diffuse into the electrolyte while discharging, and return to the interface during charging. More detailed studies are however required for higher NASICON content samples.

Fig. 3c and d, demonstrates specific charging-discharging capacitance at different rates for cells with copper and graphite collector, respectively. While discharging a small voltage drop is observed due to equivalent series resistance (ESR) of the current collector and electrode contact. The ESR with current density is calculated using the equation define below [12].

$$\text{ESR} = \frac{Voltage\ drop\ (marked\ as\ IR\ drop\ in\ graph)}{Discharge\ Curent} \quad \ldots\ldots\ldots\ldots\ldots\ (1)$$

The calculated value of ESR for the device at each current density is shown in Table 6.1. As evident, the ESR value for EDLC with graphite as a current collector shows relatively value smaller as compared to the copper collector. The results also complement the Nyquist plots (Fig. 6.2d), which suggest a better contact for activated carbon with graphite.

The specific capacitance per electrode ($F\text{-}g^{-1}$), and specific energy ($Wh\ kg^{-1}$), specific power ($W\ kg^{-1}$) for the whole device is calculated from the charging-discharging curve by considering the following Equations, also reported elsewhere [13].

$$\text{Specific capacitance } (C_s) = \frac{2I\,\Delta t}{m\Delta V} \quad \ldots\ldots\ldots\ldots\ldots\ldots\ldots\ (2)$$

$$\text{Specific energy } (E_s) = \frac{0.5Cs\Delta V^2}{7.2} \quad \ldots\ldots\ldots\ldots\ldots\ldots\ldots\ldots\ldots\ldots\ldots\ldots\ldots\ (3)$$

$$\text{Specific power } (P_s) = \frac{3600\ s}{\Delta t} \quad \ldots\ldots\ldots\ldots\ldots\ldots\ldots\ldots\ldots\ldots\ldots\ (4)$$

Where, I is the constant discharge current, Δt the discharging time, ΔV the voltage window excluding IR drop, and m is the average weight of the active material deposited on a single electrode. Interestingly, the specific discharge capacitance for cell with copper collector is found to be as high as 44 F-g^{-1} at 1.4 A-g^{-1}. The value however decreases with an increase in the current density.

Similar behavior is observed for cells with graphite collector, however, the specific discharge capacitance is found to be higher than copper collector at a similar current density (2 A-g^{-1}). Specific discharge capacitance for cell with graphite collector at a current density of 1 A-g^{-1} is found to be 104 F-g^{-1}. To summarize, specific capacity, specific energy and specific power for EDLC cell with different current collectors are shown in Table 6.1.

Table 6.1 Calculated values of the Equivalent series resistance (ESR,), specific capacitance (Cs), specific energy (Es) and specific power (Ps) (From Fig. 3c and d) at different discharge current densities. The error bars has been considered as ± 5 F-g^{-1}, ± 5 Wh Kg^{-1} ± 5 kW Kg^{-1} respectively for C_s, E_s, and P_s.

Graphite collector					**Copper collector**				
Current density (A-g^{-1})	**ESR (Ω)**	**Cs (F-g^{-1})**	**Es (Wh Kg^{-1})**	**Ps (kW Kg^{-1})**	**Current density (A-g^{-1})**	**ESR (Ω)**	**Cs (F-g^{-1})**	**Es (Wh Kg^{-1})**	**Ps (kW Kg^{-1})**
1	878	104	22	0.9	2	715	22	3	1.2
2	406	96	18	1.7	1.8	844	30	4	1.1
3	233	76	10	2.2	1.6	956	32	5	1
4	148	58	6	2.7	1.4	1128	44	7	0.7

The gravimetric charging-discharging curve at a current density of 2 A-g^{-1} with cycles is shown in Fig. 6.4a for cell with copper collector. Similarly, for the cell with graphite collector, the charging-discharging curve at a current density of 1 A-g^{-1} is shown in Fig. 6.4b. The specific charging-discharging capacity with cycle number is shown in Fig. 6.5a and b for cell with copper and graphite as collector, respectively. The inset of Fig. 6.5 shows specific discharge

capacity with number of cycles. These cells were studied up to 400 cycles and as seen, exhibit appreciable stability of the interface.

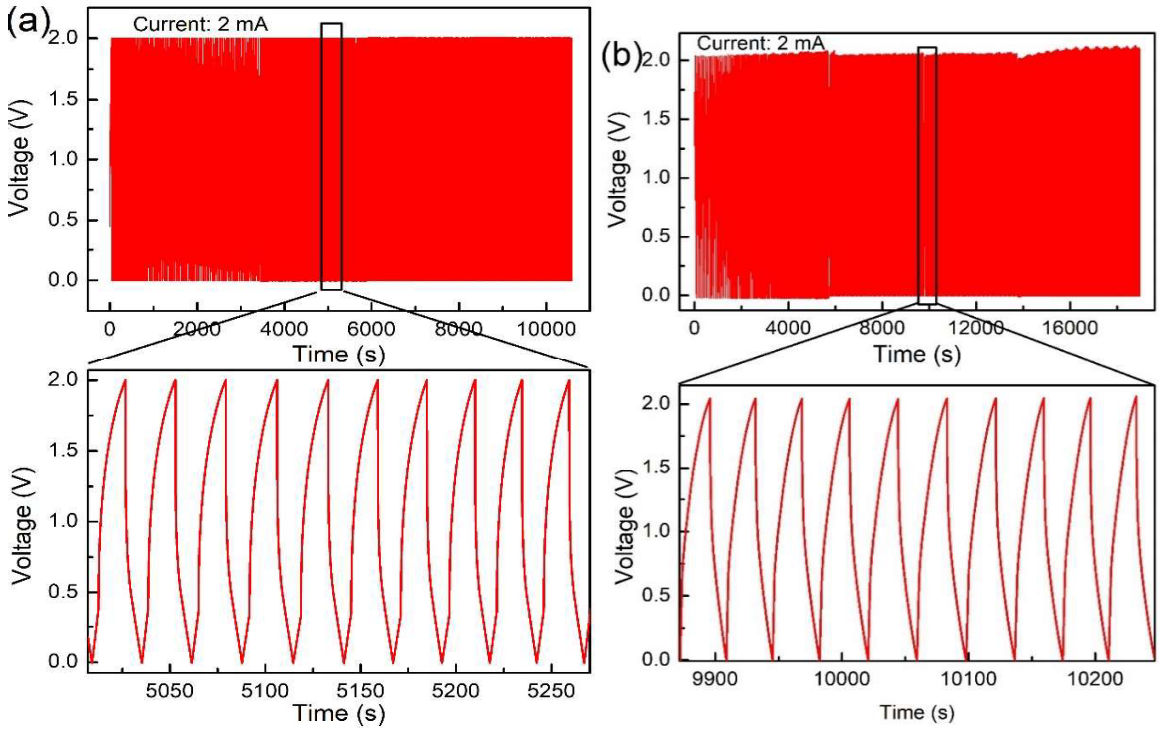

Fig. 6.4 *Galvanostatic charge-discharge curves up to 400 cycles for EDLCs with 40 NZSP composite as electrolyte with (a) copper and (b) graphite current collector. Both the cells were discharged at an actual current of 2 mA.*

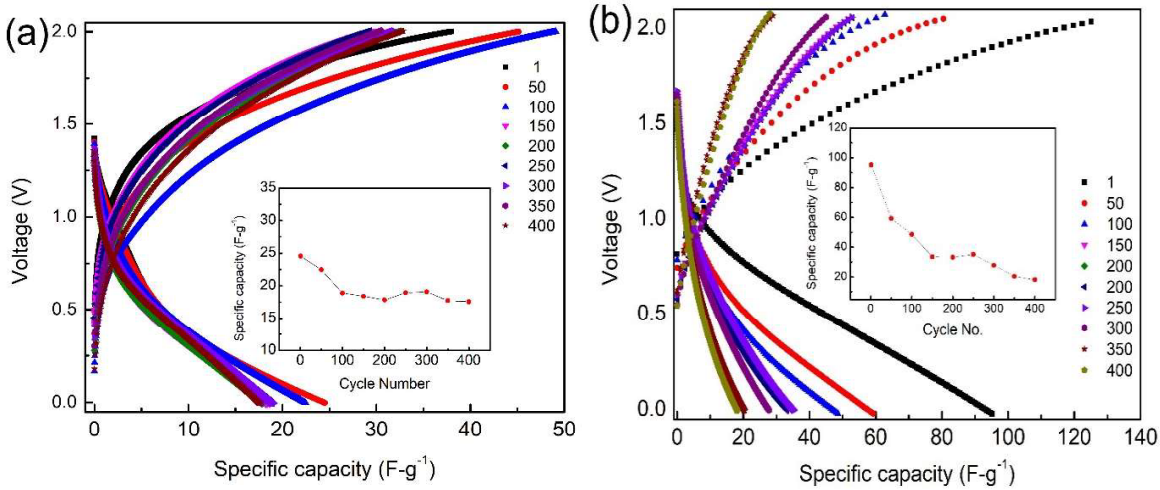

Figure 6.5 *Specific charge-discharge capacitance of the EDLCs with 40 NZSP composite as electrolyte and current collectors viz. (a) copper and (b) graphite. Inset: Specific discharged capacitance with cycle number.*

6.2. Pseudo Capacitor

In the current section, some preliminary investigations on the pseudocapacitor are discussed. Using polymer-NASICON nanocomposite of adequate conductivity (~ 10^{-5} $\Omega^{-1}cm^{-1}$) of 10NaI-90[$PEO_{0.6}NZSP_{0.4}$], pseudocapacitors were fabricated in 2032 cell with configuration as MWCNT:MnO_2 (1:1)|| 10NaI-90[$PEO_{0.6}NZSP_{0.4}$]|| MWCNT:MnO_2 (1:1), where MWCNT is multi wall carbon nanotubes, and NZSP is $Na_3Zr_2Si_2PO_{12}$.

6.2.1 MWCNT: MnO_2 electrode

Manganese oxide is a promising electrode material for the supercapacitor because of its potential to undergoes fast redox reaction [14]. However, the application of MnO_2 as an electrode in supercapacitors is limited due to low electrical conductivity. Recent studies reveal that incorporation of CNT in MnO_2 enhanced the electrical properties and thus makes it a suitable electrode for ASSCs application.

Fig. 6.6a, b and c show the XRD, Raman shift, and FESEM of the composite respectively. As evident in Fig. 6.6a, the graphitic nature of CNT is confirmed by the sharp peak center at (2θ) 26.4 and 42.5 which is due to diffraction from the (002) and (110) planes of the multi-walled carbon nanotubes [15]. The broaden peak at 23.8, 37.2, and 42.7 (of 2θ) is respectively due to diffraction from the (120), (131), and (300) planes of the γ MnO_2 [16]. As evident in Fig. 6.6a, the formation of MWCNT composite with γ MnO_2 is confirmed by the presence of suppressed peak correspond to (002) planes of MWCNT and (131) plane of γ MnO_2. The peak suppression corresponding to MWCNT (002) in the composite, and the presence of (131) plane of γ MnO_2 thus confirm the growth of γ MnO_2 in MWCNT via nucleation process from $KMnO_4$ precursor [16].

Fig. 6.6b shows the Raman spectra of the pristine MWCNT and composite. As evident, for pristine MWCNT, three prominent peaks are observed at 1326 cm^{-1}, 1576 cm^{-1}, and 2644 cm^{-1}, which corresponds respectively to the D, G, and G′ bands of MWCNT [17]. After MWCNT-MnO_2 composite formation, the appearance of one additional peak centered at 580 cm^{-1} is attributed to the symmetrical Mn–O vibration of γ phase of MnO_2 [18]. This readily confirms the incorporation of MnO_2 nanoparticles into the MWCNT [17].

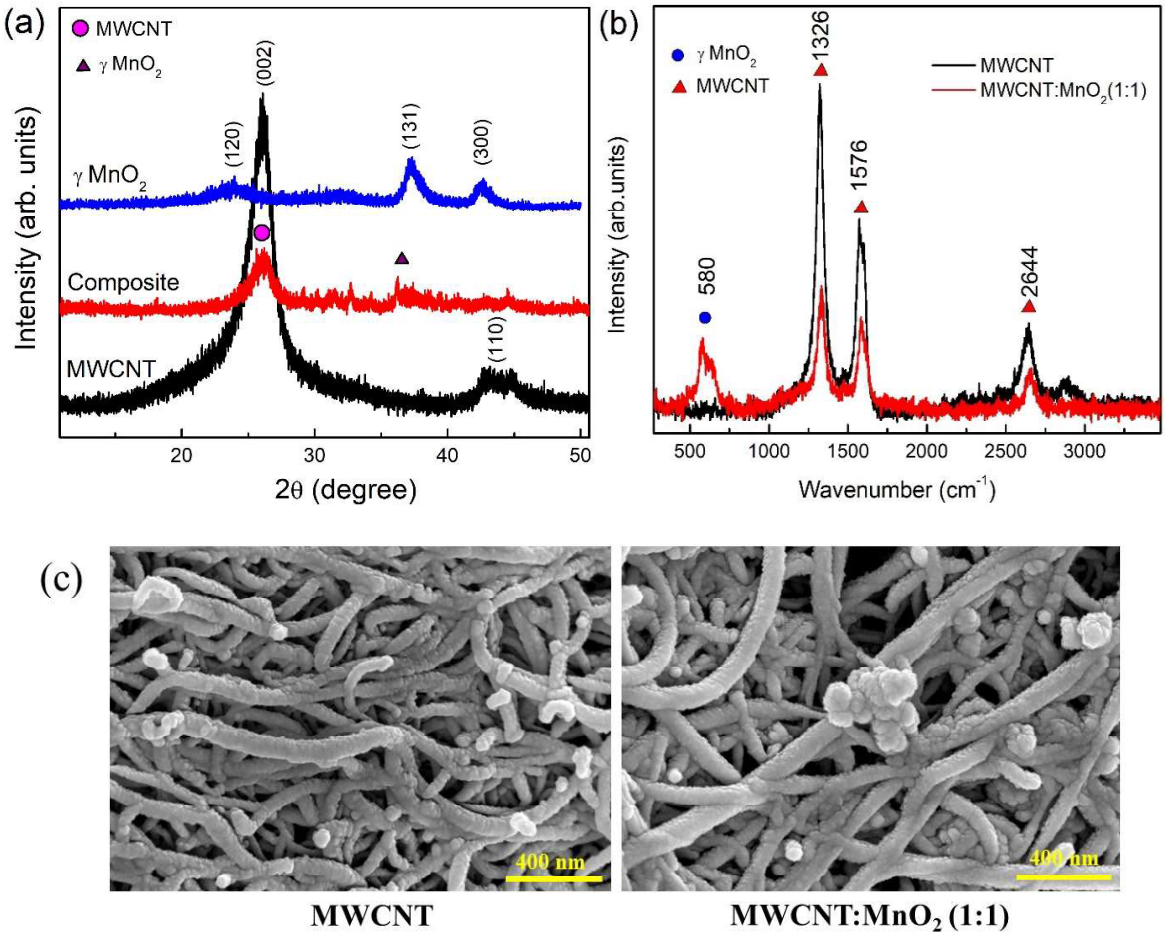

Figure 6.6 *(a) XRD patterns of pristine MWCNT, MnO2, and MWCNT-MnO2. (b) Raman spectra of pristine MWCNT and MWCNT-MnO2 composite. (c) FESEM images of pristine MWCNT and MWCNT-MnO2 composite.*

Figure 6.6c shows FESEM images of pristine MWCNT and MWCNT-MnO_2 composite. As observed in Fig. 6.6c, the FESEM image of MWCNT shows a clear random arrangement of carbon nanotubes. However, the image of the MWCNT-MnO_2 composite apparently shows the attachment of MnO_2 to the carbon nanotubes. These results again complement the MWCNT-MnO_2 formation.

6.2.2 Cell performance

The electrochemical cell performance was studied at 40°C. Fig. 6.7 shows the Nyquist plot for the cell with MWCNT-MnO_2 (1:1) as an electrode, while the inset of Fig. 6.7 shows that of the

cell with MnO_2 as an electrode. As evident in the figure, the cell with MWCNT-MnO_2 as an electrode exhibits less contact resistance (R_{ct}) as compared to the cell with MnO_2 as an electrode. The cell performance was further studied using CV.

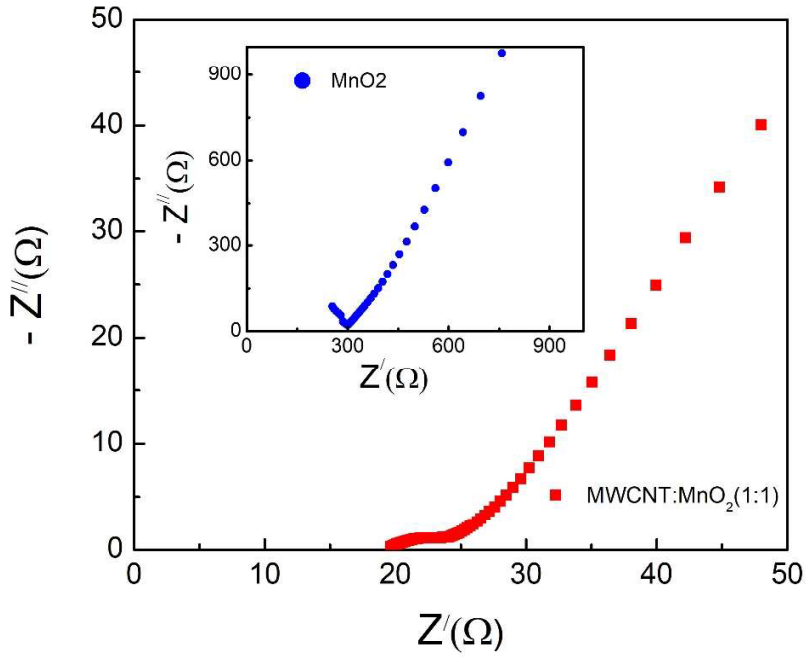

Figure 6.7 *Nyquist plot for cell with configuration of MWCNT:MnO_2 (1:1)|| 10NaI-90[$PEO_{0.6}NZSP_{0.4}$]|| MWCNT:MnO_2 (1:1). Inset shows for the cell with configuration of MnO_2|| 10NaI-90[$PEO_{0.6}NZSP_{0.4}$]||MnO_2.*

Fig. 6.8a and b shows CV cycle at a fairly smaller rate of 1 mV-s^{-1}, and also the same at different scan rates. Further, galvanostatic charge-discharge curve for cell with a configuration of MWCNT:MnO_2|| 10NaI-90[$PEO_{0.6}NZSP_{0.4}$]|| MWCNT:MnO_2 are also shown in Fig. 6.8c. The CV scan at a sweep rate of 1 mV-s^{-1} within a potential window of 0 - 0.8V confirms the Mn^{3+}/Mn^{4+} redox reaction. As evident, the CV scan exhibits a wide oxidation peak, suggesting a typical behavior of pseudo supercapacitor [19].

Further, to understand the electrochemical performance of the cell at different sweep rates, the CV curves of the samples were obtained at scan rates 10, 100, and 200 mV s^{-1} (Fig. 6.8b). At higher rates, the redox reaction is not detectable as also observed by others. As the scan rate increases, the CV maintains a quasi rectangular shape that indicates appreciable capacitive performance. The CV curves are highly reproducible as well.

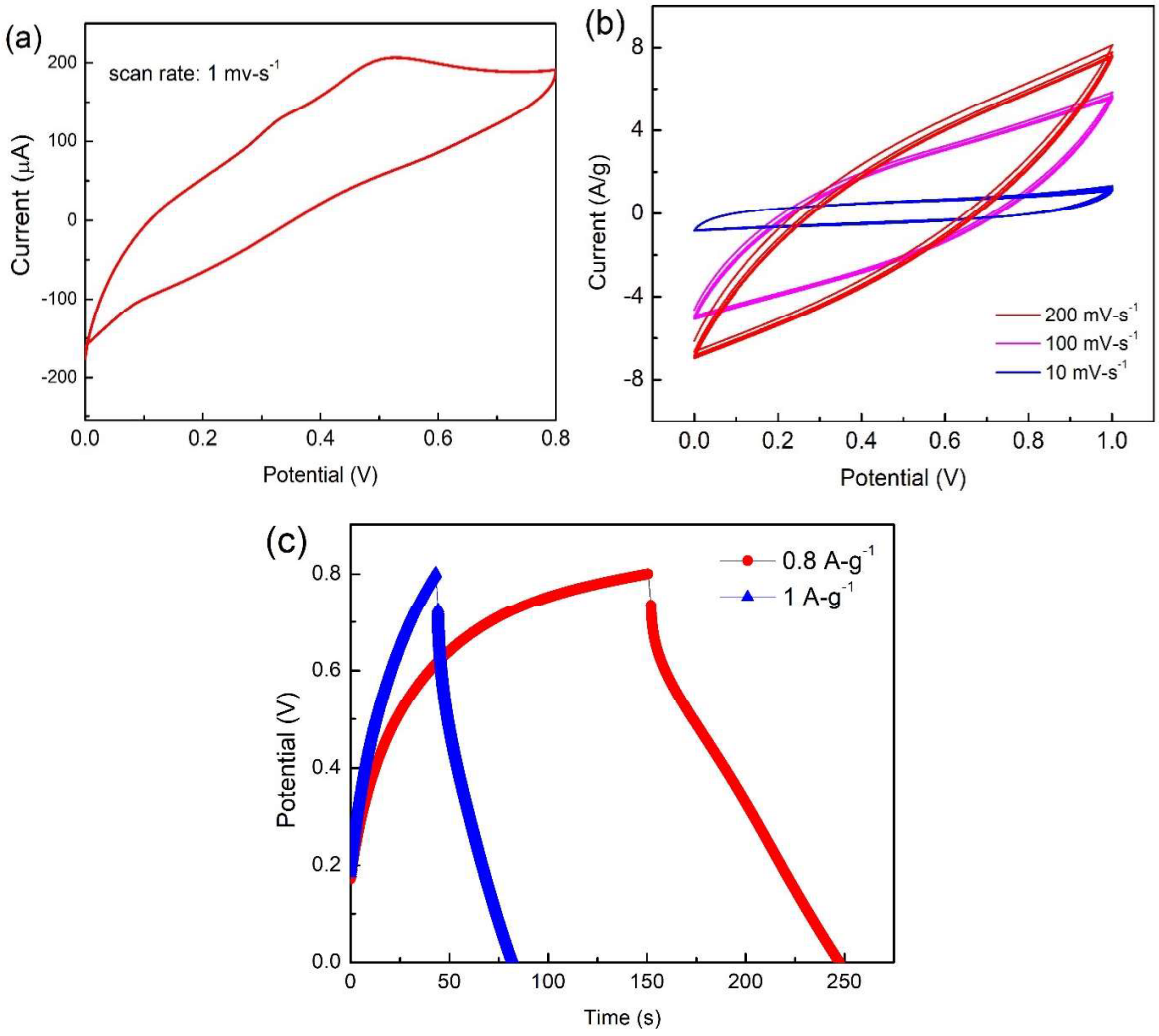

Figure 6.8 *(a) CV scan at 1 mV-s^{-1}, (b) CV scan at different sweep rate and (c) galvanostatic charge-discharge curve for cell with configuration of MWCNT:MnO_2 (1:1)|| 10NaI-90[$PEO_{0.6}NZSP_{0.4}$]|| MWCNT:MnO_2 (1:1) at a discharge current of 1 mA and 0.8 mA.*

Fig. 6.8c shows a galvanostatic charging-discharging curve at two currents densities of 1A-g^{-1} and 0.8 A-g^{-1}. As evident, while discharging a small voltage drop is observed due to equivalent series resistance (ESR) at the current collector and electrode contact. Using equation 1-4, the equivalent series resistance (ESR), specific capacitance (Cs), specific energy (Es), and specific power (Ps) for 1 A-g^{-1} and 0.8 A-g^{-1} current density values are calculated and given in Table 6.2.

Table 6.2 Calculated values of the Equivalent series resistance (ESR), specific capacitance (Cs), specific energy (Es) and specific power (Ps) (From Fig. 6.8) at different discharge current densities. The error bars are noted as ± 2 $F\text{-}g^{-1}$, ± 2 $Wh\ Kg^{-1}$ ± 2 $kW\ Kg^{-1}$ respectively for C_s, E_s, and P_s.

Current density ($A\text{-}g^{-1}$)	ESR (Ω)	Cs ($F\text{-}g^{-1}$)	Es ($Wh\ Kg^{-1}$)	Ps ($W\ Kg^{-1}$)
0.8	70	203	15	580
1	80	102	7	681

A comparison of EDLC and pseudo supercapacitor is shown in Table 6.3. A composite 40 NZSP was used as electrolyte in both devices. Pseudo exhibits lower operating voltage but higher discharge capacity.

Table 6.3 Calculated values of the specific capacitance (Cs), specific energy (Es) and specific power (Ps) for cell with 40 NZSP as electrolyte at $1A\text{-}g^{-1}$ discharge current.

Performance	EDLC	Pseudo
Operating voltage (V)	2	0.8
Specific capacity ($F\text{-}g^{-1}$)	44	102
Power density ($kW\text{-}Kg^{-1}$)	0.7	0.6
Energy density ($Wh\text{-}Kg^{-1}$)	7	7

6.3 Summary

i. Hybrid Na^+ ion NZSP-polymer composites with conductivity ~ 10^{-4}-10^{-5} Ω^{-1} cm^{-1} at room temperature are found to be suitable for ASSC applications.

ii. All the ASSCs fabricated using the Na^+ ion flexible solid electrolyte exhibit appreciable storage capacity.

iii. The NASICON content significantly influences cell performance. The 40 NZSP composites exhibit a higher energy storage capacity as compared to 0 NZSP composite.

For the highest ionic conductivity (70 NZSP composite), the cell performance is not as expected and requires further studies. Possibly, the presence of NASICON in high content leads to high contact resistance due to poor interface.

iv. At a 2V of operating voltage, EDLC cells with 40 NZSP exhibit a maximum specific capacitance of 104 $F\text{-}g^{-1}$ at a current density of 1 $A\text{-}g^{-1}$. In addition, it also shows high specific energy and specific power of 22 Wh kg^{-1} and 0.9 kW kg^{-1}, respectively.

v. Appreciable cycling stability is seen at least up to 400 cycles for EDLCs.

vi. Results also suggest that graphite is more suitable as a current collector for such EDLCs applications.

vii. At a 0.8V of operating voltage, pseudocapacitor cells with 40 NZSP exhibit a maximum specific capacitance of 203 $F\text{-}g^{-1}$ at a current density of 0.8 $A\text{-}g^{-1}$. In addition, it also shows high specific energy and specific power of 15 Wh kg^{-1} and 580 W kg^{-1}, respectively

viii. Though preliminary findings are only reported, ASSCs in pseudo-type exhibit a better cell storage capacity as compared to EDLC type.

References:

[1] G.P. Pandey, S.A. Hashmi, Y. Kumar, Performance studies of activated charcoal based electrical double layer capacitors with ionic liquid gel polymer electrolytes, Energy and Fuels. 24 (2010) 6644–6652. https://doi.org/10.1021/ef1010447.

[2] S.A. Borghei, M.H. Zare, M. Ahmadi, M.H. Sadeghi, A. Marjani, S. Shirazian, M. Ghadiri, Synthesis of multi-application activated carbon from oak seeds by KOH activation for methylene blue adsorption and electrochemical supercapacitor electrode, Arab. J. Chem. 14 (2021) 102958. https://doi.org/10.1016/j.arabjc.2020.102958.

[3] E.P. Barrett, L.G. Joyner, P.P. Halenda, The Determination of Pore Volume and Area Distributions in Porous Substances. I. Computations from Nitrogen Isotherms, J. Am. Chem. Soc. 73 (1951) 373–380. https://doi.org/10.1021/ja01145a126.

[4] C. Lei, F. Markoulidis, Z. Ashitaka, C. Lekakou, Reduction of porous carbon/Al contact resistance for an electric double-layer capacitor (EDLC), Electrochim. Acta.

92 (2013) 183–187. https://doi.org/10.1016/j.electacta.2012.12.092.

[5] C. Peng, L. Yang, S. Fang, J. Wang, Z. Zhang, K. Tachibana, Y. Yang, S. Zhao, Electrochemical behavior of copper current collector in imidazolium-based ionic liquid electrolytes, J. Appl. Electrochem. 40 (2010) 653–662. https://doi.org/10.1007/s10800-009-0040-y.

[6] S. Sahoo, K. Krishnamoorthy, P. Pazhamalai, V.K. Mariappan, S. Manoharan, S.J. Kim, High performance self-charging supercapacitors using a porous PVDF-ionic liquid electrolyte sandwiched between two-dimensional graphene electrodes, J. Mater. Chem. A. 7 (2019) 21693–21703. https://doi.org/10.1039/c9ta06245a.

[7] F. Béguin, V. Presser, A. Balducci, E. Frackowiak, Carbons and electrolytes for advanced supercapacitors, Adv. Mater. (2014). https://doi.org/10.1002/adma.201304137.

[8] M.D. Singh, A. Dalvi, D.M. Phase, Y. Kumar, Li1.3Al0.3Ti1.7(PO4)3 reinforced hybrid polymer composites: assessment of enhanced Li+ ion transport and potential for solid-state supercapacitor applications, J. Mater. Sci. 55 (2020) 3951–3963. https://doi.org/10.1007/s10853-019-04234-9.

[9] M. Dinachandra Singh, A. Dalvi, D.M. Phase, Novel Na3Zr2Si2PO12–polymer hybrid composites with high ionic conductivity for solid-state ionic devices, Mater. Lett. 262 (2020) 127022. https://doi.org/10.1016/j.matlet.2019.127022.

[10] M. Dinachandra Singh, A. Dalvi, Ionic transport in NASICON-polymer hybrids: An assessment using X-ray photoelectron spectroscopy, Appl. Surf. Sci. 536 (2021) 147792. https://doi.org/10.1016/j.apsusc.2020.147792.

[11] B. Pal, S. Yang, S. Ramesh, V. Thangadurai, R. Jose, Electrolyte selection for supercapacitive devices: a critical review, Nanoscale Adv. 1 (2019) 3807–3835. https://doi.org/10.1039/C9NA00374F.

[12] S.R.S. Prabaharan, R. Vimala, Z. Zainal, Nanostructured mesoporous carbon as electrodes for supercapacitors, J. Power Sources. 161 (2006) 730–736. https://doi.org/10.1016/j.jpowsour.2006.03.074.

[13] Q. Xie, X. Huang, Y. Zhang, S. Wu, P. Zhao, High performance aqueous symmetric supercapacitors based on advanced carbon electrodes and hydrophilic poly(vinylidene fluoride) porous separator, Appl. Surf. Sci. 443 (2018) 412–420.

https://doi.org/10.1016/j.apsusc.2018.02.274.

[14] J. Zhu, D. Zhang, Z. Zhu, Q. Wu, J. Li, Review and prospect of MnO2-based composite materials for supercapacitor electrodes, Ionics (Kiel). (2021) 3699–3714. https://doi.org/10.1007/s11581-021-04139-1.

[15] L. Vellingiri, K. Annamalai, R. Kandasamy, I. Kombiah, Synthesis and characterization of MWCNT impregnated with different loadings of SnO2 nanoparticles for hydrogen storage applications, Int. J. Hydrogen Energy. 43 (2018) 848–860. https://doi.org/10.1016/j.ijhydene.2017.11.023.

[16] C. Wang, Y. Zeng, X. Xiao, S. Wu, G. Zhong, K. Xu, Z. Wei, W. Su, X. Lu, γ-MnO2 nanorods/graphene composite as efficient cathode for advanced rechargeable aqueous zinc-ion battery, J. Energy Chem. 43 (2020) 182–187. https://doi.org/10.1016/j.jechem.2019.08.011.

[17] S. Kasap, E. Nostar Aslan, I. Oztürk, Investigation of MnO2 nanoparticles-anchored 3D-graphene foam composites (3DGF-MnO2) as an adsorbent for strontium using the central composite design (CCD) method, New J. Chem. 43 (2019) 2981–2989. https://doi.org/10.1039/c8nj05283b.

[18] S. Cheng, L. Yang, D. Chen, X. Ji, Z. jie Jiang, D. Ding, M. Liu, Phase evolution of an alpha MnO2-based electrode for pseudo-capacitors probed by in operando Raman spectroscopy, Nano Energy. 9 (2014) 161–167. https://doi.org/10.1016/j.nanoen.2014.07.008.

[19] Y. Zhao, M. Dai, D. Zhao, L. Xiao, X. Wu, F. Liu, Asymmetric pseudo-capacitors based on dendrite-like MnO2 nanostructures, CrystEngComm. 21 (2019) 3349–3355. https://doi.org/10.1039/c9ce00423h.